

Article

# Retained Austenite Destabilization during Tempering of Low-Temperature Bainite

Victor Ruiz-Jimenez <sup>1</sup>, Matthias Kuntz <sup>2</sup>, Thomas Sourmail <sup>3</sup>, Francisca G. Caballero <sup>1</sup>,  
Jose A. Jimenez <sup>1</sup> and Carlos Garcia-Mateo <sup>1,\*</sup>

<sup>1</sup> MATERIALIA Research Group, Department of Physical Metallurgy, National Center for Metallurgical Research (CENIM-CSIC), Avenida Gregorio del Amo, 8, 28040 Madrid, Spain; vrj@cenim.csic.es (V.R.-J.); fgc@cenim.csic.es (F.G.C.); jimenez@cenim.csic.es (J.A.J.)

<sup>2</sup> Robert Bosch GmbH, Corporate Research, 71272 Renningen, Germany; matthias.kuntz2@de.bosch.com

<sup>3</sup> Ascometal Research (CREAS), BP 70045 Hagondange, France; thomas.sourmail@ascometal.com

\* Correspondence: cgm@cenim.csic.es; Tel.: +34-91-553-8900

Received: 17 November 2020; Accepted: 10 December 2020; Published: 13 December 2020



**Abstract:** The thermal stability of nanostructured microstructures consisting of a mixture of bainitic ferrite and carbon-enriched retained austenite has been studied in two steels containing 0.6 C (wt %) by tempering cycles of 1 h at temperatures ranging from 450 to 650 °C. Volume changes due to microstructural transformations during thermal treatments were measured by high-resolution dilatometry. The correlation of these results with the detailed microstructural characterization performed by X-ray diffraction and scanning electron microscope examination showed a sequence of different decomposition events beginning with the precipitation of very fine cementite particles. This precipitation, which starts in the austenite thin films and then continues in retained austenite blocks, decreases the carbon content in this phase so that fresh martensite can form from the low-carbon austenite on cooling to room temperature. In a subsequent tempering stage, the remaining austenite decomposes into ferrite and cementite, and due to carbide precipitation, the bainitic ferrite loses its tetragonality, its dislocation density is reduced, and the bainitic laths coarsen.

**Keywords:** bainite; thermal stability; atomic volumes; tempering; X-ray diffraction

## 1. Introduction

Bainitic transformation in high Si steels leads to microstructures consisting of bainitic ferrite and carbon-enriched retained austenite. When the chemical composition of the steels is adjusted so that this transformation occurs at low temperatures (150–350 °C), a structure is obtained that contains bainitic ferrite plates with a size of the order of a few tens of nm and retained austenite with two very distinctive morphologies, thin films and blocks, which also contain very different amounts of carbon in solid solution. This microstructure has been referred as superbainite, nanobain, or nanostructured bainite.

The presence of retained austenite in the microstructure can be a problem for dimensional stability in high-precision components, since it could transform to martensite in the finished item [1,2]. On the other hand, ductility and notch impact toughness are greatly influenced by carbon super-saturation in retained austenite. As reported by several studies, both the retained austenite and carbon supersaturated bainitic ferrite can be decomposed into a mixture of ferrite and cementite by a tempering process at a high enough temperature [3–11]. This process involves several reactions that often overlap and may be affected by alloying elements, which usually starts with the decomposition of C-rich austenite followed by that of the C-poor austenite and bainitic ferrite [10,12]. On the other hand, Podder and Bhadeshia [13,14] have demonstrated the existence of an intermediate stage of austenite destabilization in a medium C steel (0.22 wt %), where the precipitation of minute quantities of cementite within

austenite precedes its decomposition into ferrite and cementite, so that fresh martensite can form from the low-carbon austenite on cooling to room temperature.

With all these scenarios in mind, in this work, we undertake a detailed examination of the decomposition sequence of bainitic microstructures developed in two new designed steels containing 0.6% C and 1.7% Si (wt %), but different quantities of Mo and V, by isothermal transformation at 250 °C after austenitizing at 1150 °C [15]. These alloys are circumscribed within the new developments that are being performed to evaluate the potential of a new class of steel combining nanostructured bainitic steels with secondary precipitation. Potential applications are subjected to elevated temperatures and require high fatigue performances at these temperatures (e.g., gas injection components, bearings, gears) [15].

As retained austenite is present in an amount higher than 20%, one of the key factors in determining the tempering resistance of the bainitic microstructure is the austenite thermal stability. For this reason, we have studied the sequence of the reactions occurring during the austenite decomposition by high-resolution dilatometry, and these results have been correlated with the detailed microstructural characterization performed on a very fine scale by X-ray diffraction and scanning electron microscope examination.

## 2. Materials and Methods

Two steels containing (in wt %) 0.6% C and 1.7% Si and different amounts of carbide-forming alloying elements such as Mo and V have been designed in the frame of a new development concept of including the secondary hardening reaction under certain tempering conditions in nanostructured bainitic steels [15–18]. As shown in Table 1, these steels also include 1.3% Mn and 1.7% Cr to ensure low bainite (Bs) and martensite (Ms) start temperatures [19–21], and the high Si content ensures the absence of cementite precipitation during bainitic transformation [22].

**Table 1.** Chemical analysis (in wt %) of the steels used for this study.

	C	Si	Mn	Cr	Ni	Mo	Cu	V
<b>06CV</b>	0.6	1.7	1.3	1.7	0.2	0.2	0.2	0.5
<b>06C1MoV</b>	0.6	1.7	1.3	1.7	0.2	1.0	0.2	0.5

The materials used for this study were manufactured as laboratory cast and heat treated to obtain a nanobainitic microstructure. To achieve this microstructure, both steels were austenitized at 1150 °C and then isothermally held for 20 h at 250 °C in a molten salt bath. The starting bainitic structures were subjected to tempering treatments consisting in heating the sample at 5 °C/s up an annealing temperature ranging between 450 and 650 °C, holding for 1 h, and then cooling down to room temperature at 5 °C/s, as shown in Figure 1. Tempering heat treatments were performed in a High-Resolution Dilatometer, Bahr 805D (TA Instruments, Germany), which enables studying phase transformation by monitoring the changes in the sample length. This device uses an induction coil to heat the sample and helium flow to cool it down. Throughout the experiment, the temperature is controlled by a K-type thermocouple welded at the mid length of the sample surface. Dilatometry tests, on cylindrical samples of 4 mm diameter and 10 mm length, were performed using fused silica push-rods, and the longitudinal length changes were recorded using a linear variable differential transducer (LVDT) in contact with the pushrods.

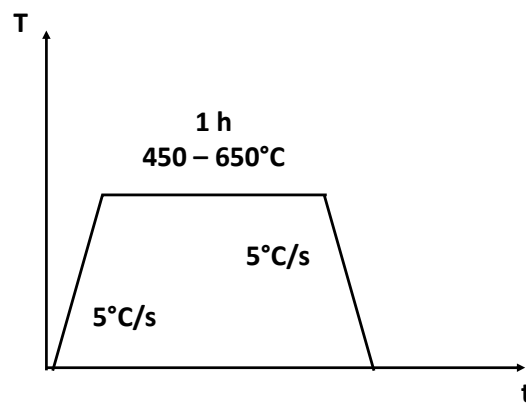


**Figure 1.** Scheme of the tempering heat treatments applied in this work.

Metallographic preparation was performed using a standard procedure that included grinding with SiC papers up to 1200 grit, and polishing in the final step with diamond paste of 3 and 1  $\mu\text{m}$ . The different microstructures were revealed by etching the polished surfaces with a 2% Nital (2% nitric acid in ethanol) solution and observed in a FEG-SEM Hitachi S48000 microscope operating at an accelerating voltage of 7 kV. In the case of the samples used for X-Ray diffraction, additional polishing and etching cycles were introduced to avoid the presence of martensite transformed from austenite on the surface of the sample during the metallographic preparation. X-ray diffraction (XRD) patterns were recorded using a Bruker AXS D8 diffractometer equipped with a Co X-ray tube working at 40 kV and 30 mA, a Goebel mirror, and a LynxEye Linear Position Sensitive Detector (Bruker AXS, GmbH, Karlsruhe, Germany). Coupled  $\theta$ - $2\theta$  scans were carried out over a  $2\theta$  range of  $35$ – $135^\circ$  with a step size of  $0.01^\circ$ . The full diffraction patterns obtained were refined using the 4.2 version of Rietveld analysis program TOPAS (Bruker AXS) and the crystallographic information of the different phases (ferrite, austenite, and cementite) for quantitative phase analysis. In addition to global parameters such as background, zero displacement, and scale factors, the refinement protocol also included the unit-cell parameters by the double Voigt approach [23]. For this analysis, a corundum sample was used to remove the instrumental contribution to the width of the diffraction peaks.

Theoretical calculations by means of atomic volumes were performed in order to later assist on the interpretation and understanding of the changes detected on the dilatometric curves. It is known that changes in the volume fraction of individual phases during phase transformations can be determined through careful analysis of contractions and/or expansions in the dilatometric signal as a function of time or temperature [12,24]. On the other hand, the change in carbon content leads to a change in the atomic volume of austenite, which makes the austenite dilatometric curve deviate from linearity. As will be described later in this manuscript, during tempering, different scenarios can be simulated in which the initial bainitic microstructure, which is composed of bainitic ferrite ( $\alpha_b$ ) and retained austenite ( $\gamma_r$ ), might evolve toward its equilibrium, ferrite ( $\alpha$ ) and cementite ( $\theta$ ).

The procedure used for the theoretical calculations is based on the determination of the volume variation ( $\Delta V$ ) between the initial ( $V_{ini}$ ) and final ( $V_{fin}$ ) state of the microstructure, taking into account the unit cell volume of the different phases ( $V_i$ ) and their corresponding fraction ( $f_i$ ), where subscript  $i$  stands for the phase. All calculations were performed in this work under the assumption of isotropic dilatation behavior, where the relative change in volume ( $\Delta V/V_{ini}$ ) is directly related to  $\Delta L/L_{ini}$  by

$$\Delta V/V_{ini} = (1 + \Delta L/L_0)^3 - 1 \approx 3\Delta L/L_{ini}.$$

The atomic volumes of the phases involved in these calculations are given in Table 2 as a function of their lattice parameter, while Table 3 gathers the composition dependence at room temperature of the different lattice parameters (note that in the case of cementite, the lattice parameters are considered unique). As the mentioned calculations are intended at a given tempering temperature,

it is imperative to correlate the room temperature lattice parameters,  $a_0$ , with those expected at the tempering temperature,  $a_i(T)$ . Therefore, it was necessary to use the thermal expansion coefficients ( $\beta_i$ ) shown in Table 2, in expressions of the type  $a_i(T) = a_0(1 + \beta_i(T - 25))$  [25,26], where T is the tempering temperature.

**Table 2.** Atomic volume and thermal expansion coefficients of the different phases used in this work where  $a_i$ ,  $b_i$ , and  $c_i$  are the lattice parameters and  $\beta_i$  represents the thermal expansion coefficients.

Crystal Structure	Unit Cell Atomic Volume	$\beta_i$ ( $^{\circ}\text{C}^{-1}$ )	Ref.
$\gamma$ (fcc)	$a_i^3/4$	$2.065 \cdot 10^{-5}$	[13]
$\alpha_b$ (bct)	$a_i^2 c_i/2$	$1.490 \cdot 10^{-5}$	[27]
$\alpha$ (bcc)	$a_i^3/2$	$1.244 \cdot 10^{-5}$	[13]
$\theta$ (Orthorhombic)	$a_i b_i c_i/12$	$6 \cdot 10^{-6} + 3 \cdot 10^{-9} T + 10^{-11} T^2$	[28,29]

**Table 3.** Theoretical lattice parameters of the different phases at room temperature, where w is the concentration in weight%, x in mole fraction and  $a_{Fe} = 2.88664$  is the lattice parameter of pure ferrite.

	Lattice Parameter ( $\text{\AA}$ ) at Room T	Ref.
$\gamma$ (fcc)	$a = 3.578 + 0.033 w_C + 0.00095 w_{Mn} - 0.0002 w_{Ni} + 0.0006 w_{Cr} + 0.022 w_N + 0.0056 w_{Al} - 0.0004 w_{Co} + 0.0015 w_{Cu} + 0.0031 w_{Mo} + 0.0051 w_{Nb} + 0.0039 w_{Ti} + 0.0018 w_W + 0.0018 w_W$	[30]
$\alpha_b$ or $\alpha'$ (bct)	$a = 2.8664 - 0.01303 \cdot w_{C\alpha}$ $c = 2.8664 + 0.1162 \cdot w_{C\alpha}$	[31]
$\alpha$ (bcc)	$a_{Fe} + \frac{(a_{Fe} - 0.279 x_C)^2 (a_{Fe} + 2.496 x_C) - a_{Fe}^3}{3 \cdot a_{Fe}^2} - 0.03 x_{Si} + 0.06 x_{Mn} + 0.07 x_{Ni} + 0.31 x_{Mo} + 0.05 x_{Cr} + 0.096 x_V$	[26]
$\theta$ (Orthorhombic)	$a = 4.5246$ $b = 5.0885$ $c = 6.7423$	[28,29]

In addition, Vickers hardness measurements of the different microstructures obtained with isothermal treatments applied were performed according to ASTM E92 [32] standard using a 30 kg load; reported values correspond to an average of at least three measurements. Finally, the experimental results on the evolution of the microstructure during tempering were compared with the theoretical calculations carried out using MTDATA (National Physical Laboratory, Teddington, UK) [33] commercial software together with the SGTE database for steels to determine the equilibrium phase distribution at different tempering temperatures.

### 3. Results

#### 3.1. Initial Microstructure

Microstructural characterization of the as-received material confirmed the presence of a nanobainitic microstructure in both alloys consisting of a matrix of bainitic ferrite plates ( $\alpha_b$ ) and retained austenite. As shown in Figure 2, two austenite morphologies can be differentiated: thin films ( $\gamma_f$ ) sandwiched between bainite ferrite plates and islands of untransformed residual austenite between the sheaves of bainite, which is blocky in nature ( $\gamma_b$ ). Although austenite will be enriched in C ( $C_\gamma$ ) during austempering, experimental observations had shown that austenite films can be more so because of their geometrical isolation between plates of ferrite [34–36]; the relevance of such will become clear later in this manuscript.

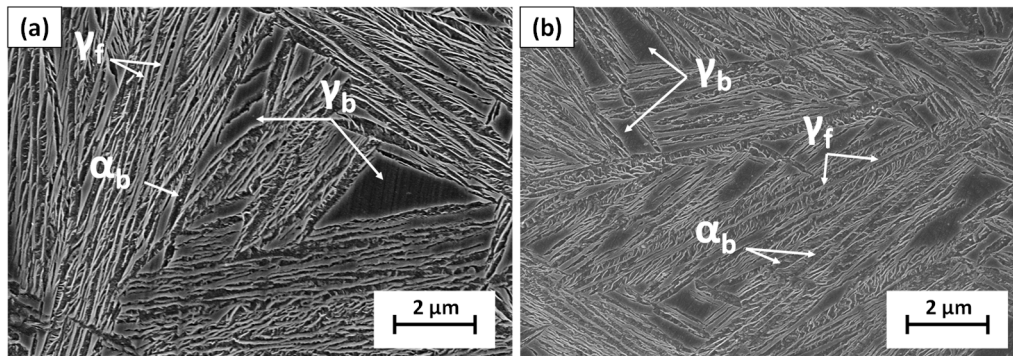


**Figure 2.** SEM micrographs of bainitic microstructures obtained after isothermal transformation at 250 °C for 20 h in (a) 06CV and (b) 06C1MoV steels, where  $\alpha_b$  stands for bainitic ferrite and  $\gamma$  stands for retained austenite with film (f) and block (b) morphology.

The results of the Rietveld refinement performed on XRD patterns obtained for as-received conditions and their Vickers hardness values are summarized in Table 4. This table shows that the greatest difference observed between both materials lies in a greater volume fraction of retained austenite ( $f_\gamma$ ) for the 06C1MoV steel, while the carbon content in bainitic ferrite ( $C_{ab}$ ) and austenite ( $C_\gamma$ ) and the Vickers hardness (HV) are almost identical for both steels.

**Table 4.** Fraction and carbon content of retained austenite ( $f_\gamma$ ,  $C_\gamma$ ) and bainitic ferrite ( $f_{\alpha_b}$ ,  $C_{\alpha_b}$ ) obtained from XRD, and hardness results for the initial bainitic microstructures.

Steel	$f_\gamma$ ( $\pm 0.03$ )	$C_\gamma$ ( $\pm 0.06$ wt %)	$f_{\alpha_b}$ ( $\pm 0.03$ )	$C_{\alpha_b}$ ( $\pm 0.03$ wt %)	HV30
06CV	0.23	0.90	0.77	0.18	596 $\pm$ 3
06C1MoV	0.32	0.91	0.68	0.20	601 $\pm$ 2

It should be noted that a carbon content as high as 0.2 wt % in solid solution in bainitic ferrite has been previously reported in high C and high Si bainitic steels, resulting in the appearance of a tetragonal distortion in the ferritic lattice [37–40]. Finally, the formation of cementite from austenite during bainitic transformation has not been detected in any of the two steels studied (with the characterization techniques used in this work), even after many hours at the isothermal transformation temperature [41–43]. This absence of cementite formation is expected due to the presence of an Si content higher than 1.5 wt %.

### 3.2. Selection of Tempering Conditions

Dilatometric tests were performed to record the relative change in length (RCL) and its derivative (DRCL) during the continuous heating of the bainitic microstructures from room temperature to the fully austenitic field. As can be seen in Figure 3, RCL vs. temperature dilatometric data show clearly a linear thermal expansion characteristic in the two temperature ranges where no phase transformation occurred, which correspond to the regions of  $\alpha_b + \gamma_r$  and single austenitic phase, respectively. Moreover, two main change stages were identified in the DRCL curve (more sensitive to microstructural changes than the RCL curve) at around 550 and 800 °C, which correspond with decomposition of the bainitic microstructure and the austenitization of the tempered microstructure, respectively. These peaks are negative, which means that a contraction of the matrix occurred during both processes. Finally, it was noteworthy that before starting the second transformation, we observed an inflection in the RCL at about 745 °C, which is marked by a red arrow in Figure 3a. This change was associated to the Curie temperature, because in Figure 3b, there is an observed a change in the DRCL that corresponds to the spontaneous magnetostriction that occurs below the Curie temperature.

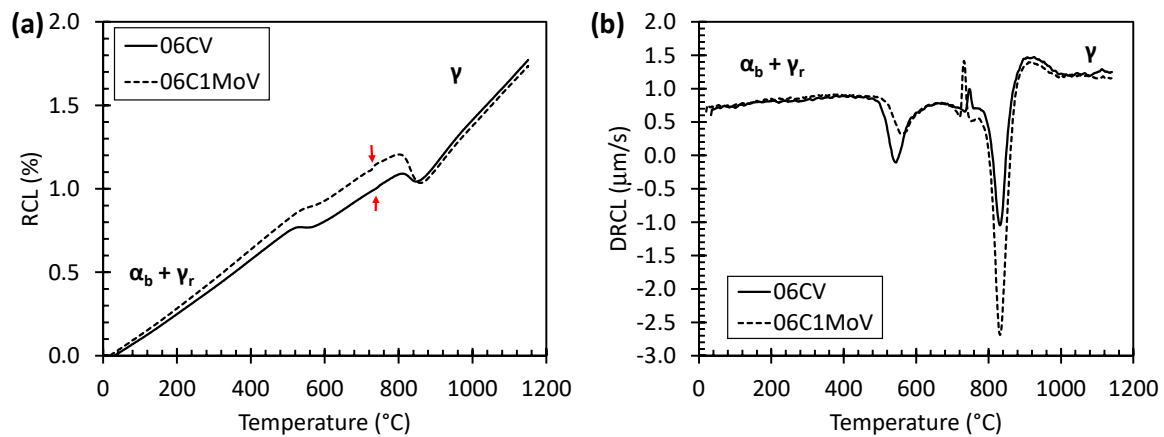


**Figure 3.** Dilatometry results of (a) relative change in length and (b) first derivate during a continuous heating up to austenitization temperature for all steels.

As the key factor in determining the tempering resistance of a bainitic microstructure is the austenite thermal stability, it is expected that steel 06C1MoV containing a higher amount of retained austenite in its microstructure presents a higher deviation from the baseline in the DRCL curve in the peak at lower temperature region. However, Figure 3b shows that the peak corresponding to the austenite decomposition (around 500 °C) presents a higher area for the 06CV steel. The peak temperature of this reaction for this steel occurs at a lower temperature than for the 06C1MoV steel. As the major difference among the studied steels is their Mo content, it was concluded that a high Mo addition has improved the strong effect of V on the temper resistance of steels by slowing down the tempering reactions and the size of carbides that precipitate during tempering [44–46]. In order to separate the reactions occurring during the retained austenite decomposition, tempering experiments were constrained in the range between 450 and 650 °C in steps of 50 °C.

### 3.3. Dilatometric Study of the Microstructural Evolution during Tempering

In this section, the dilatometry results obtained during the isothermal tempering treatments performed are analyzed in detail, and an attempt to establish the sequence by which the microstructure decomposes is made. For this, a first set of generic theoretical calculations based on atomic volumes was carried out to later help in the interpretation of the RCL curves. Considering the previous knowledge about the tempering behavior of martensite and bainite [3,6–10,47–57], and the fact that the initial microstructure is composed of carbon-rich ferrite and austenite, which both will tend to equilibrium during the tempering process, the following possible scenarios, as schematically presented in Table 5, are studied:

1. Retained austenite decomposes into a mixture of ferrite and cementite,  $\gamma (fcc) \rightarrow \alpha (bcc) + \theta$ . These calculations took into account the fact that the austenite retained in the bainitic microstructure has two distinctive morphologies that are characterized by containing very different levels of C in solid solution [34–36]. Therefore,  $C_\gamma$  was varied between that of the bulk (no C enrichment) and 2.5 wt %, which is a typical C enrichment detected for thin films of retained austenite [34–36].
2. Before the decomposition described above, it could occur that part of the austenite goes through an intermediate state where it releases part of its C saturation due to the precipitation of the cementite particles [13,14], which are mostly rich in Fe but also with a certain amount of Cr and Mo:  $\gamma (fcc) \rightarrow \gamma^- (fcc) + \theta$ . The calculations for this scenario are made from the XRD results shown in Table 4 for the 06C1MoV alloy.
3. The excess of C in bainitic ferrite can be released as cementite precipitates, leading to the progressive loss of tetragonality of the bainitic ferrite and finally reaching its equilibrium as a bcc phase,  $\alpha_b (bct) \rightarrow \alpha (bcc/bct) + \theta$ . The initial C content of bainitic ferrite,  $C_{ab}$ , is assumed to be

0.2 wt %, which is in accordance with both the XRD results presented in Table 4 and previous experiences with similar microstructures [37–40].

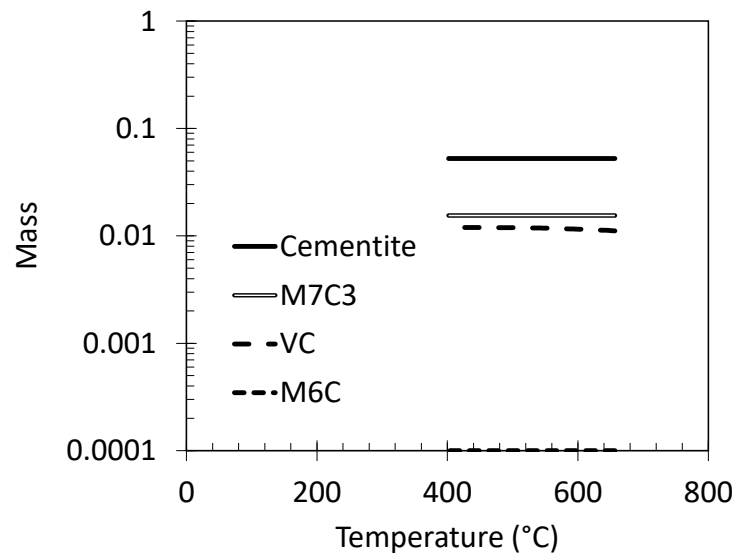
- Finally, the possibility is considered that some of the C from the supersaturated bainitic ferrite could be transferred to the retained austenite in a similar way to what happens during Q&P or Q + T processes. The calculations for this scenario are made from the XRD results shown in Table 4 for the 06C1MoV alloy. In this case, it must be considered that there are no changes in the fractions of the phases involved:  $\gamma + \alpha_{bct}^+ \rightarrow \gamma^+ + \alpha_{bct}^-$ .

**Table 5.** Conditions used to calculate by atomic volumes the relative change in length (RCL) and the fraction of the phases involved in the mentioned scenarios occurring during a tempering treatment. The signs – and + denotes more or less C as compared to the initial state, respectively.

State	Phases	Conditions ( $C_i$ (wt %))
Scenario 1 $\gamma$ (fcc) $\rightarrow$ $\alpha$ (bcc) + $\theta$		
Initial	$\gamma$	$C_\gamma = 0.6\text{--}2.5$
Final	$\alpha$ (bcc)	$C_\alpha = 0.03$
	$\theta$	$C_\theta = 6.67$
Scenario 2 $\gamma$ (fcc) $\rightarrow$ $\gamma^-$ (fcc) + $\theta$		
Initial	$\gamma$	$C_\gamma = 0.91$
Final	$\gamma^-$	$C_{\gamma^-} = 0.9\text{--}0.7$
	$\theta$	$C_\theta = 6.67$
Scenario 3 $\alpha_b$ (bct) $\rightarrow$ $\alpha$ (bct/bcc) + $\theta$		
Initial	$\alpha_b$ (bct)	$C_{\alpha_b} = 0.2$
Final	$\alpha$ (bct/bcc)	$C_\alpha = 0.03$
	$\theta$	$C_\theta = 6.67$
Scenario 4 $(\gamma + \alpha_b \rightarrow \gamma^+ + \alpha_b^-)$		
Initial	$\gamma$	$C_\gamma = 0.91$ $f_\gamma = 0.32$
	$\alpha_b$ (bct)	$C_{\alpha_b} = 0.2$ $f_{\alpha_b} = 1 - f_\gamma = 0.68$
Final	$\gamma^+$	$C_{\gamma^+} = [f_\gamma(C_\gamma - C_{\alpha_b} + C_{\alpha_b^-}) + (C_{\alpha_b} - C_{\alpha_b^-})] / f_\gamma$ $f_{\gamma^+} = f_\gamma$
	$\alpha_b^-$ (bct)	$C_{\alpha_b^-} = 0.2\text{--}0.1$ $f_{\alpha_b^-} = f_{\alpha_b}$

On tempering at temperatures higher than 550 °C, precipitation of VC and M<sub>7</sub>C<sub>3</sub>, and also M<sub>6</sub>C in the steel containing Mo, carbides may occur simultaneously due to secondary hardening and carbide precipitation from austenite. Although the precipitation of these types of carbides during tempering can have a strong influence on the kinetics and the temperature range of the tempering reactions, its effect on the volume changes that occur during tempering can be neglected due to the relatively small content of these carbides that should be present in the microstructure compared to cementite. Figure 4 shows the equilibrium mass fraction of carbides as a function of the tempering temperature calculated using the MTDATA (National Physical Laboratory, Teddington, UK) together with the SGTE database for the chemical composition of the steel used for this study. As the mass fraction expected

for these carbides is about 0.01%, they would not be easy to detect by XRD. On the other hand, due to the depletion of carbon content by carbide precipitation, the Ms of any retained austenite remaining in the material increases, so that it can transform into martensite on cooling.



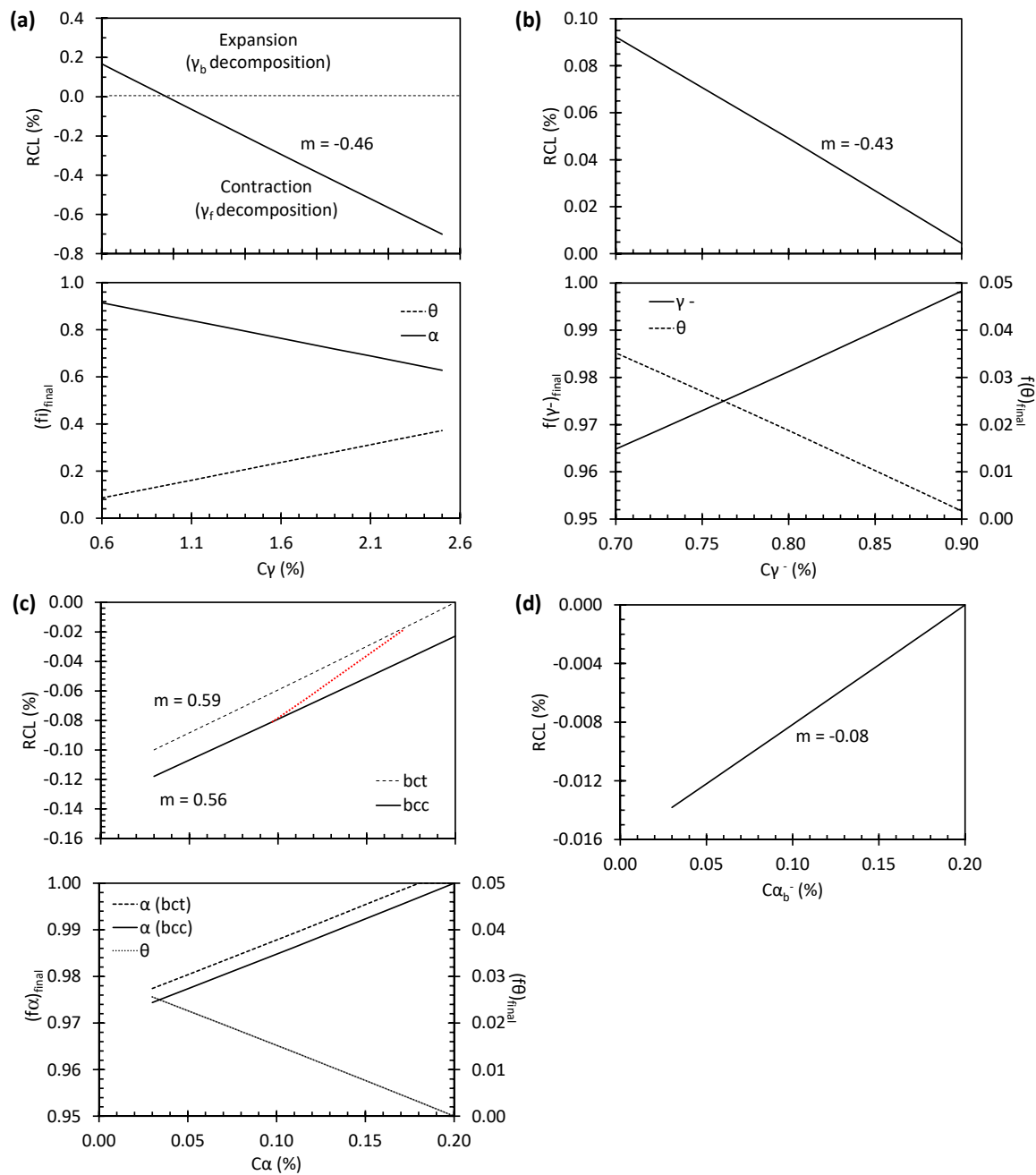
**Figure 4.** Calculated equilibrium mass fractions of carbides as a function of tempering temperature.

Table 5 presents a summary of the different conditions used in the described scenarios. In accordance with the procedures described in the previous sections, the chemical compositions of the 06C1MoV steel and a tempering temperature of 550 °C were selected for the atomic volume calculations. The constraints given in Equation (1) were applied for scenarios 1, 2, and 3, while those of Equation (2) were applied for scenario 4. In both equations, the subscript  $i$  indicates the phase and  $f_i$  and  $C_i$  indicate its fraction and C content respectively, and the term  $ini$  and  $fin$  refers to the initial and the final state, as indicated in Table 5.

$$\begin{aligned} 1 &= (\sum f_i)_{fin} \\ (C_i)_{ini} &= (\sum f_i C_i)_{fin} \end{aligned} \quad (1)$$

$$\begin{aligned} (f_i)_{ini} &= (f_i)_{fin} \\ (\sum f_i C_i)_{ini} &= (\sum f_i C_i)_{fin} \end{aligned} \quad (2)$$

A summary of the results thus obtained is given in Figure 5, where values of the  $RCL > 0$  and  $RCL < 0$  correspond to expansions and contractions, respectively. It should be noted according to the calculations shown in Figure 5a that the decomposition of austenite would produce for scenario 1 an expansion for a C content less than 1.1 wt %, while a contraction is expected for higher values of  $C_\gamma$ , which agrees with previous observations [58–60]. This, in principle, would allow establishing a distinction in the decomposition behavior of the C-rich thin films ( $\gamma_f$ ) and C-poor blocks ( $\gamma_b$ ) of retained austenite present in the initial microstructure; see Figure 2. The fractions of  $\alpha$  and  $\theta$  resulting from the decomposition of retained austenite estimated from these calculations are shown in Figure 5a. Then, it is clear that a maximum fraction of 0.10 of  $\theta$  could be expected from the initial fraction of retained austenite if its complete decomposition is assumed.



**Figure 5.** Theoretically calculated relative change in length (RCL) and volume fraction of relevant phases involved in the different scenarios described in the main text and detailed in Table 5, (a) scenario 1, (b) scenario 2, (c) scenario 3, and (d) scenario 4. The slope of the RCL as function of carbon content is reported as m.

In scenario 2, as shown in Figure 5b, the partial release of saturated austenite C in the form of cementite precipitates leads to an expansion of the system. However, the amount of cementite that is formed in this scenario is always very small.

As shown in Figure 5c, it is expected for scenario 3 that tetragonal bainitic ferrite decomposes realizing the C supersaturation as  $\theta$  precipitates:  $\alpha_b$  (bct)  $\rightarrow$   $\alpha$  (bcc) +  $\theta$ . Since the majority of the carbon atoms in solid solution within bainite is at dislocation sites, before precipitation can occur, some dislocations must be removed by recovery, but the presence of carbon strongly inhibits recovery [57,61,62].  $\theta$  carbide precipitation from bainite is very sluggish and occurs gradually as

the tempering temperature is increased. This process is accompanied by a progressive loss of its tetragonal character, and the final structure consists of cementite and a “defect-free” bcc ferrite matrix. In Figure 5c, the red dotted line exemplifies the transition between the bct toward the bcc line.

Finally, the result of the calculations made for scenario 4 is represented in Figure 5d. This figure shows how a partial enrichment of the retained austenite with C from the supersaturated bainitic ferrite results in system shrinkage, but its order of magnitude is too small compared to the other scenarios. Therefore, it can be assumed that if this mechanism were to occur, it would be overshadowed by any of the other scenarios or that it is not detectable by dilatometry. Figure 6 shows the dilatometry curve obtained during isothermal tempering at 350 °C. It can be observed a length increase of about 0.01% after 1 h of tempering, but as changes in the microstructure were neither expected nor detected by XRD and HV measurements, it can be attributed to the relaxation of compressive stresses built up during quenching from the austenitizing treatment to the austempering temperature or even to the uncertainty in the RCL measurement. In any case, this scenario has been considered highly unlikely, at least at tempering temperatures up to 450 °C, since no such enrichment of carbon, from ferrite to austenite, was detected by 3D atom probe tomography [57].

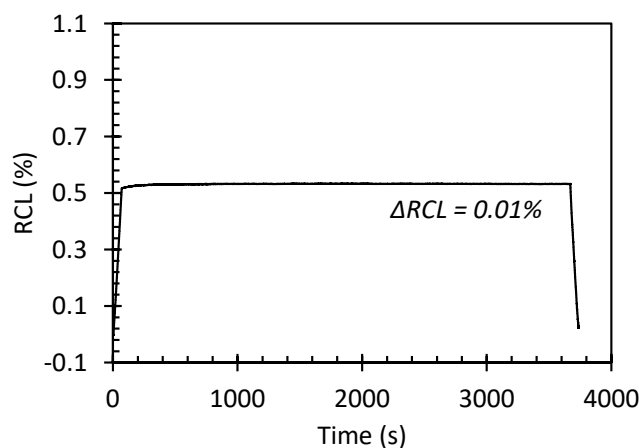


**Figure 6.** Relative change in length (RCL) as a function of time for 06CV steel tempered at 350 °C.

Additional information on the evolution of the microstructure during the entire tempering treatment can be obtained by analyzing in detail the dilatometry curves obtained. Illustrative examples of these curves as a function of the tempering temperature and the treatment time are given in Figure 7 only for the 06C1MoV steel, since the behavior of both steels is equivalent. Although Figure 3 showed that no changes occur during heating at temperatures below 500 °C, Figure 7a and b illustrate a contraction in the RCL during isothermal holding at 450 and 500 °C, respectively. In the case of the sample held at 450 °C, the RCL decreased progressively up to  $-0.03\%$ , but for the sample held at 500 °C, the RCL decreased  $-0.06\%$  after 1300 s and then reached a plateau. It is likely that the microstructural changes associated with this shrinkage of the samples are related to the partial decomposition of the C-enriched austenite films according to scenario 1, since its higher content of C gives them a greater driving force for carbide precipitation [6–8,10,13,14].

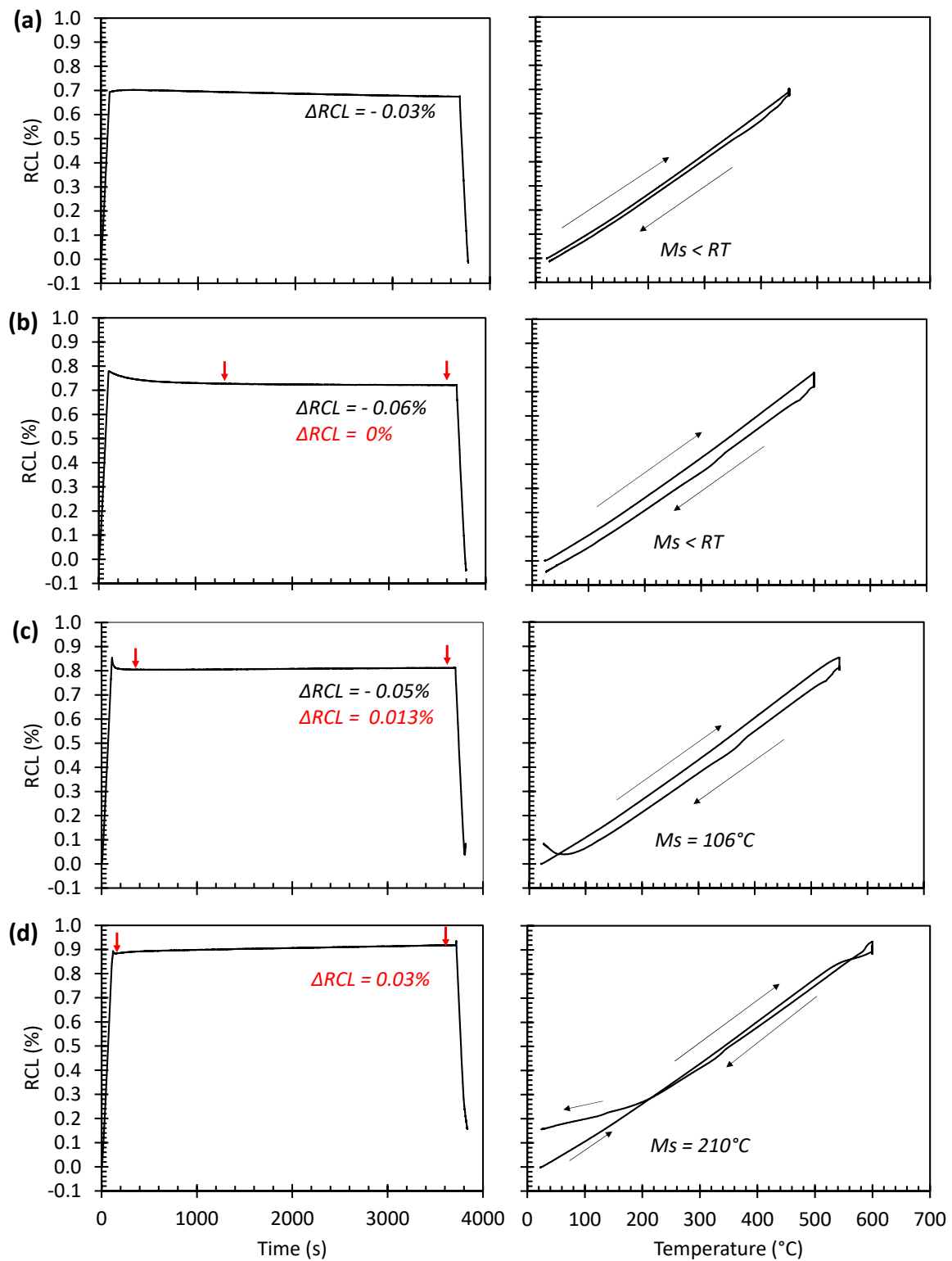


**Figure 7.** Relative change in length (RCL) as a function of time and temperature for 06C1MoV steel tempered at (a) 450 °C, (b) 500 °C, (c) 550 °C, and (d) 600 °C.

During tempering at 550 and 600 °C, an RCL decrease occurred, which was followed by a length increase that is more pronounced at 600 °C, as shown in Figure 7c,d. Austenite films begin to decompose during heating to these holding temperatures, so once isothermal holding begins, the carbide precipitation process triggered in scenario 1 is quickly over. Comparing the RCL curves

of Figure 7c,d, it can be concluded that an increase of 50 °C in the tempering temperature leads to a significantly lower reduction in length and a decrease in the time required for carbide precipitation.

The increase in length observed in the RCL curve after the initial contraction is compatible with the decomposition of the remaining retained austenite depleted in C by both scenarios 2 and 1. However, the RCL curve recorded during cooling to room temperature after the isothermal treatment at 500 and 600 °C shows that some austenite transformed to fresh martensite. The appearance of a martensitic transformation during cooling means that the amount of carbon in austenite has been reduced continuously during isothermal tempering by the precipitation of carbides (scenario 2). As shown in Figures 7 and 8, the measured Ms temperature decreases as the tempering temperature is increased, indicating that martensite is produced from an austenite with a lower C content.

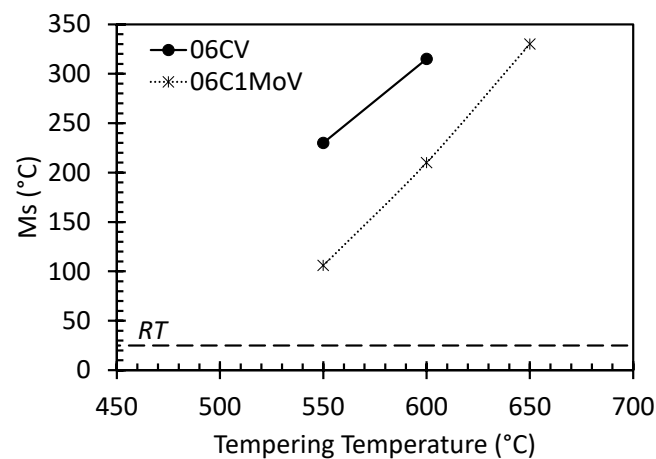


**Figure 8.** Measured Ms temperatures on cooling after tempering at the indicated temperature.

The hypothesis that the austenite decomposition sequence begins with scenario 2 and ends with scenario 1 is reinforced by the dilatometric results shown in Figure 9 for the tempering treatment at 650 °C. It can be observed that RCL curves increases during isothermal holding at this temperature, revealing that scenario 1 for C-rich films and the possible loss of the tetragonality of the ferrite (scenario 3) have already occurred during heating. For the 06CV steel, the appearance of a plateau in the RCL curve after 0.08% expansion and the absence of any length change related to the martensitic transformation during cooling to room temperature would indicate that the austenite decomposition has been completed during isothermal tempering. On the contrary, the austenite decomposition of the 06C1MoV steel is not completed after 1 h at 650 °C, since the RCL curve does not reach a plateau, and there is some C impoverished austenite available to transform to martensite during cooling. These results would indicate that the addition of Mo delays the kinetics of the reactions that take place during tempering.

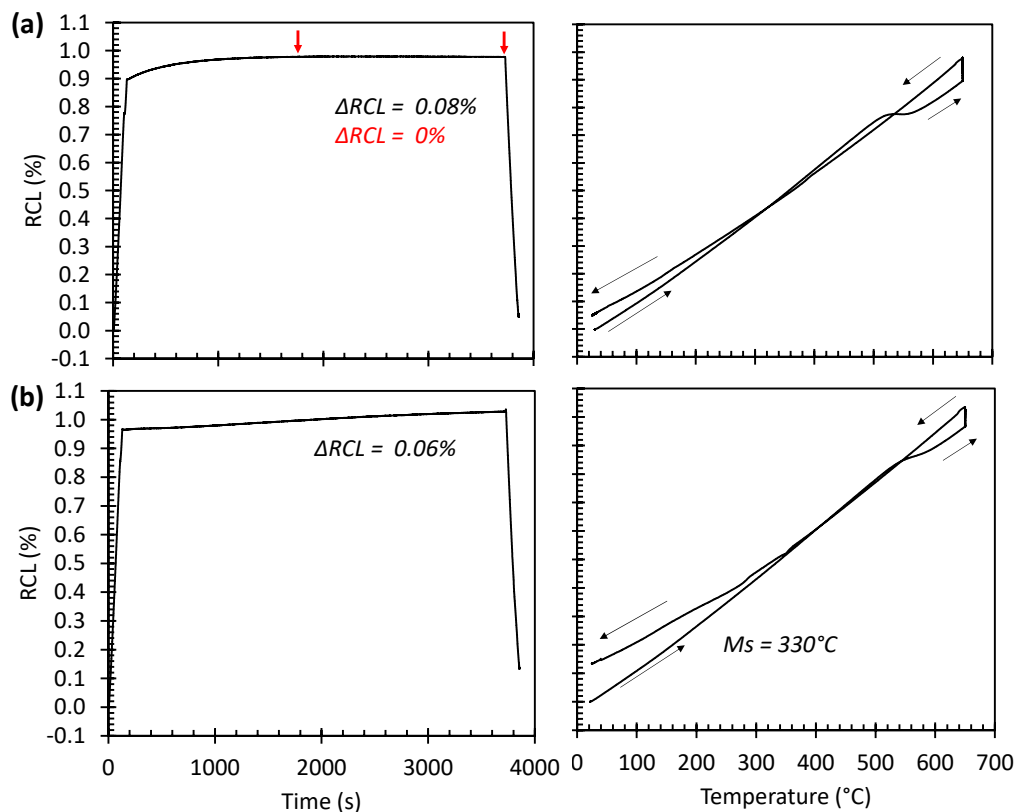


**Figure 9.** Relative change in length (RCL) as a function of time and temperature for (a) 06CV and (b) 06C1MoV steel tempered at 650 °C.

### 3.4. Microstructural Characterization of Tempered Microstructures by XRD and SEM

The results of the above dilatometry tests were correlated with a detailed microstructural characterization to evaluate the influence of the tempering temperature on the thermal stability of the nanostructured microstructures present in both steels. FEG-SEM micrographs of the microstructure developed after isothermal holding for 1 h showed a very similar tendency for both steels. Thus, only representative microstructures are given in Figure 10 for the 06CV steel after tempering at temperatures ranging from 450 to 650 °C. Figure 11 gathers the XRD results for the tempered microstructures. As anticipated by dilatometry results, Figure 10a (450 °C tempering) shows the same microstructure to that found in Figure 2. On the other hand, the XRD parameters deduced from the Rietveld refinement for both as received and tempered materials are basically the same as deduced from Figure 11. Tempering at 450 °C does not introduce perceptible changes in the microstructure, and retained austenite with both thin-film and blocky island morphologies remains basically unchanged, indicating that this temperature is not high enough for its transformation.

The behavior of the steels differs during tempering at 50 °C. As shown in Figure 11, while 06C1MoV steel still does not present any appreciable changes in their microstructure, the 06CV steel already exhibits signs of austenite decomposition, as its fraction decreases by 0.12 as compared to the initial microstructure and the previous treatment at 450 °C. The decomposition of the austenite is accompanied by the precipitation of carbide particles, but the XRD pattern of this sample did not show any diffraction peak of cementite. The low symmetry of cementite causes a greater number of reflections in the diffraction pattern. The distribution of the scattered X-rays in many directions decreases the intensity of a single peak, and the nanometric sizes, microstrain, and faulting of the carbide particles broadens the reflections. The combination of both effects strongly affects the limit of detection (LoD) of the cementite present in a sample, which decreases to a value ranging from 3 to 5 wt %. As a reference, the LoD for retained austenite for same measurement conditions is about 1 wt % in a low alloyed

steel. Although the bainitic ferrite plates and the retained austenite blocks remain unchanged after tempering for 1 h at 500 °C, Figure 10b evidences by red arrows the precipitation of fine cementite particles in the location where retained austenite films were originally present. This microstructural evolution during tempering would agree with the decomposition of austenite films described for scenario 1. The remaining austenite is still sufficiently C-enriched to remain stable at room T, and no fresh martensite formation was detected during cooling in the RCL curve of Figure 7.

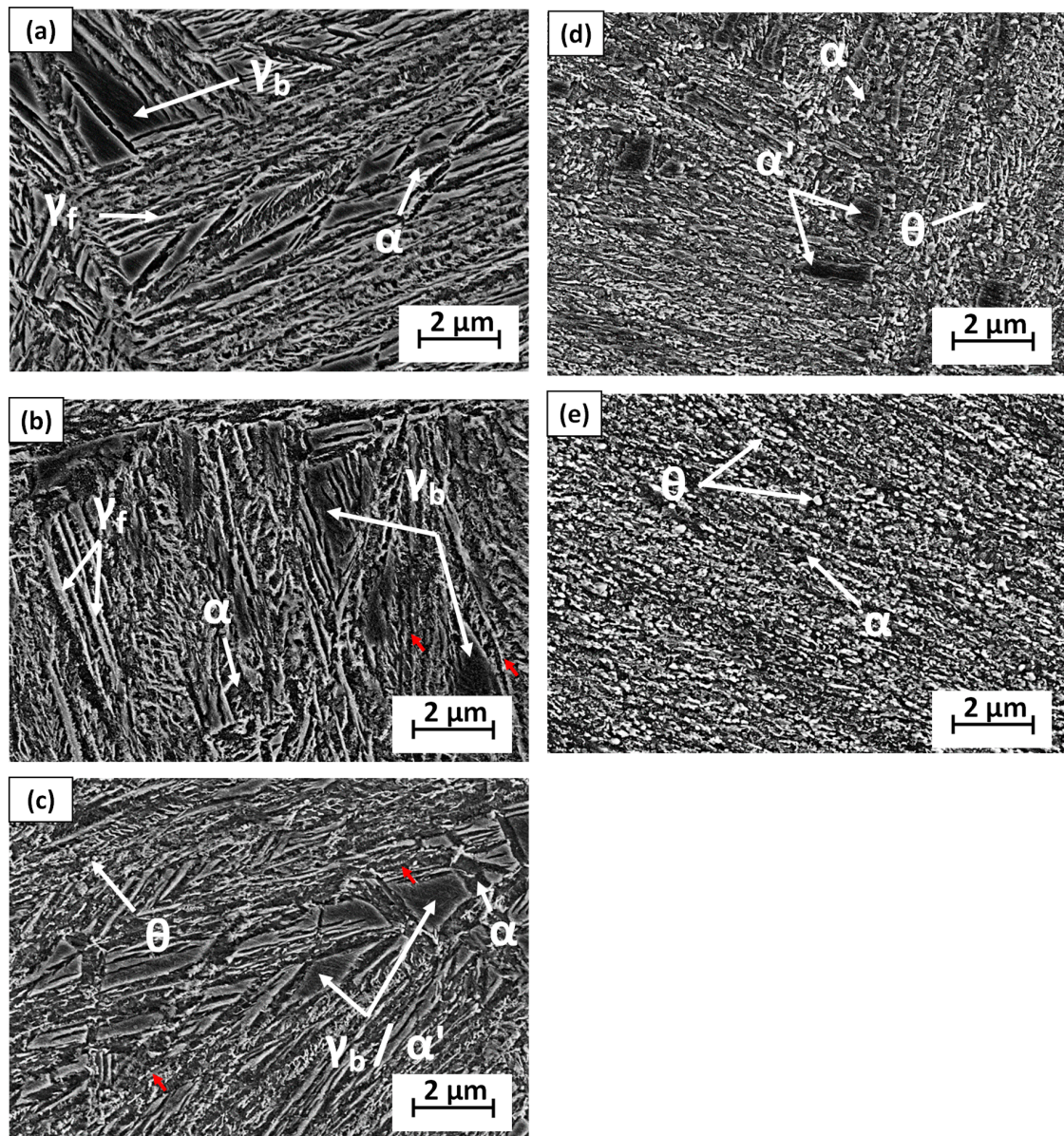


**Figure 10.** SEM micrographs after tempering for 1 h at (a) 450 °C, (b) 500 °C, (c) 550 °C, (d) 600 °C, and (e) 650 °C in the case of 06CV steel.

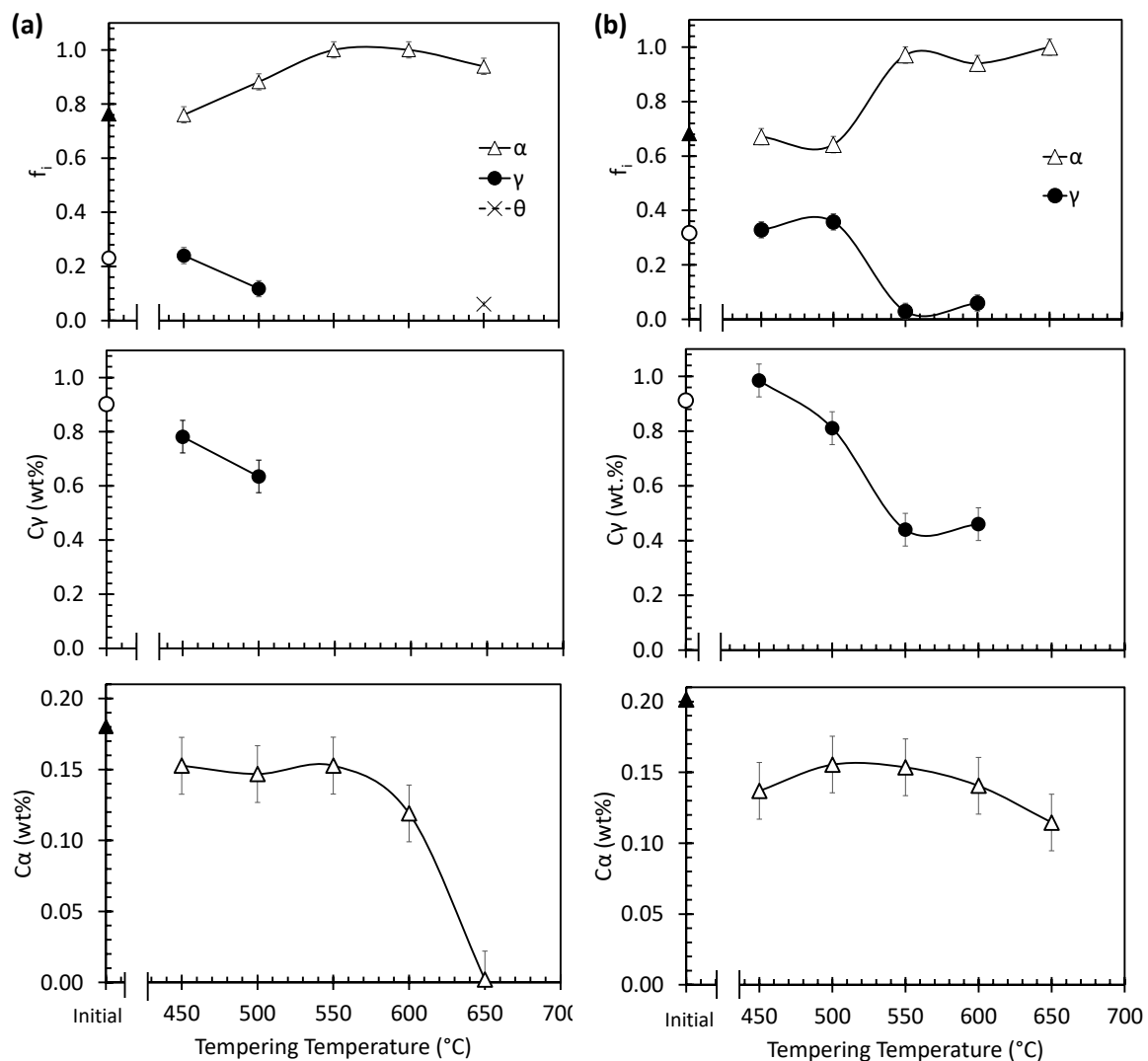


**Figure 11.** Summary of XRD results as a function of tempering temperature for (a) 06CV and (b) 06C1MoV steel.

The higher tempering resistance at 500 °C of the 06C1MoV microstructure compared to 06CV is also evident for the other tempering conditions. As previously shown in the dilatometry results, increasing tempering temperatures leads to greater decomposition of the bainitic microstructures. Although no austenite was detected in their XRD patterns, Figures 7 and 8 show for the 06CV steel the transformation to martensite of a certain amount of austenite during cooling to room temperature after tempering at 550 and 600 °C, which indicates that the decomposition of austenite was not complete. When Figure 10a is compared with Figure 10c,d, it is observed that the number and size of the blocky features decrease as the tempering temperature increases. On the other hand, fresh martensite within the block structures can also be observed in a closer look at these figures as a result of the transformation of the retained austenite during cooling. Although martensitic transformation is also detected during cooling after tempering at 550 and 600 °C for 06C1MoV in Figures 7 and 8, Figure 11b shows the presence of 5% and 3% austenite retained at room temperature. Note that the XRD measurements were done after cooling to room temperature, and therefore, the microstructure already contains fresh transformed martensite.

For 06C1MoV steel, Figures 8 and 9 show the formation of martensite during cooling after tempering at 650 °C and Figure 11b shows the absence of retained austenite in the microstructure, indicating that austenite was depleted in C to levels that make it unstable at room temperature. On the

other hand, the full decomposition of the retained austenite for the 06CV steel during tempering at this temperature is concluded by the lack of martensitic transformation in Figures 8 and 9 and austenite in Figure 11b. The decomposition of retained austenite and the precipitation of carbides in this case are evident in the profuse precipitation observed in Figure 10e, so that the presence of cementite was detected in the XRD patterns only in this case, but it was below their limit of quantification (LoQ).

Although the XRD reflections of the ferritic phase ( $\alpha$ ) may include the contribution of bainitic ferrite ( $\alpha_b$ ), ferrite ( $\alpha$ ), and martensite ( $\alpha^-$ ), the largest information obtained from these reflections corresponds to bainitic ferrite, since this phase represents around 70% of the initial microstructure. Bainitic ferrite decomposition follows scenario 3, and therefore, increases in tempering temperature should lead to a progressive decrease in the average  $C_\alpha$ . As shown in Figure 11c, the C content of this phase is very similar and remains almost constant after tempering up to 550 and 600 °C for the 06CV and 06C1MoV steels, respectively. These results agree with those of Jang et al., who, based on the first principles calculations, suggests that ferrite in equilibrium with austenite has much higher carbon solubility if it displays tetragonal crystalline symmetry instead of cubic [40]. As the maximum solubility is achieved at about 400 °C and extends over a long temperature range, carbon excess will have a high resistance due to being released from bainitic ferrite during tempering in this temperature range. It has been experimentally proved that up to 0.2 wt % can be in solid solution within ferrite and trapped at dislocations sites and bainite lath boundaries [1], since the dislocations density near these boundaries are usually much higher than in the lath interior [63]. The complete decarburization of supersaturated ferrite [57,61] requires the precipitation of carbide from C trapped in dislocations [62], but for this some dislocations must be removed by recovering during tempering. As carbon is more stable while segregated to dislocations than in transition carbides or cementite [62], the high dislocation density is then stabilized by carbon pinning, causing the recovery of the dislocation network to be strongly inhibited. Thus, the tetragonal structure of bainitic ferrite will be stable up to high tempering temperatures [8,10], as shown in Figure 11.

The evolution of the hardness values as a function of the tempering temperature has been correlated with the microstructural evolution described previously. Figure 12 shows that up to 450 °C, hardness remains unchanged, within an error margin of  $\pm 10$  HV30, for both steels, as expected from the microstructural stability observed in this temperature range. As soon as the decomposition of the austenite thin films and the precipitation of the cementite begin, a progressive increase in the hardness curve is observed until reaching a maximum between 500–550 and 550 °C for the 06CV and 06C1MoV steels, respectively. An additional contribution to this maximum value comes from the martensite that transforms from austenite after tempering during cooling to room temperature, as observed in Figures 7 and 8.

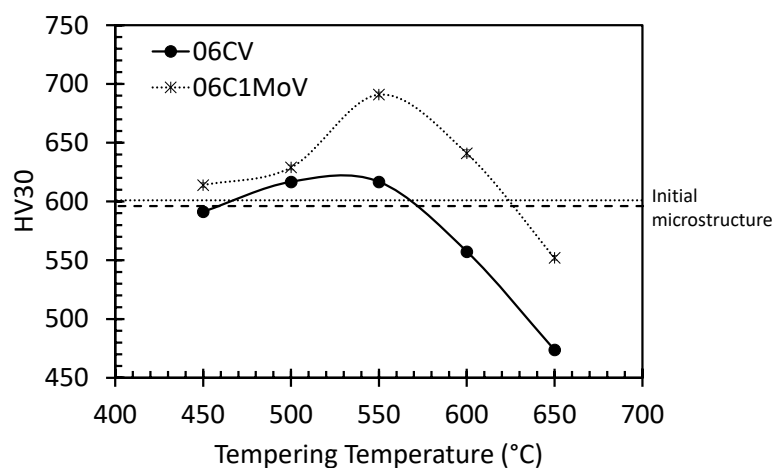


Figure 12. HV ( $\pm 10$ ) results as a function of tempering temperature.

The decrease in the hardness value observed in Figure 12 for higher tempering temperatures is accompanied by two simultaneous processes: the continuation of the decomposition of austenite, which leads to the precipitation of carbide and the decrease of the C content in the remaining retained austenite, and the recovery of bainite plates, which leads to a reduction in the carbon content in solid solution by carbide precipitation and a reduction of the dislocation density of the bainitic ferrite and a coarsening of the bainitic laths. As austenite is dispersed in the bainitic ferrite matrix and the bainite represents more than 70% of the microstructure, hardness should be principally associated with the contribution of this phase. On the other hand, the strengthening associated to carbide precipitation from the austenite and the transformation to martensite of the austenite during cooling should increase the hardness value. Thus, it was concluded that in this tempering temperature range, the contribution of austenite decomposition to the hardness value is rather limited, and the microstructural evolution of the bainite during the thermal treatment described before would explain the hardness value achieved.

#### 4. Conclusions

The complementary use of high-resolution dilatometry, XRD analysis, microstructural observations, and hardness measurements allowed obtaining a clear picture on the different events that occurs in a bainitic microstructure composed of fine bainitic ferrite plates and thin films and blocks of retained austenite during tempering at temperatures ranging from 450 to 650 °C. This study shows that all processes occurring during tempering are related to the carbide precipitation, austenite decomposition, and dislocation density evolution in bainitic ferrite as well as coarsening of the bainitic laths. The scenario proposed describes the microstructural evolution as the tempering temperature is increased, which starts with the retained austenite thin films decomposing to very fine cementite particles, followed by fine precipitation of cementite within the blocks of retained austenite, while the remaining C-depleted austenite eventually decomposes into ferrite and cementite at a later stage. This particular sequence of events, where tempering resulted in a reduction in the carbon content of austenite, resulted in its partial transformation to fresh martensite on cooling to room temperature, which is unambiguously identified using high-resolution dilatometry, at temperatures as high as 600 °C.

This later stage is coupled with the decomposition of the tetragonal bainitic ferrite by carbide precipitation, which is accompanied by the reduction of the dislocation density by a recovering process and the coarsening of the bainitic laths.

**Author Contributions:** Conceptualization, All authors.; methodology, C.G.-M., M.K., F.G.C., T.S., J.A.J.; validation, V.R.-J., C.G.-M., J.A.J.; formal analysis, All authors; investigation, All authors; resources, M.K., C.G.-M.; data curation, C.G.-M., V.R.-J.; writing—original draft preparation, C.G.-M., V.R.-J.; writing—review and editing, All authors; supervision, C.G.-M.; project administration, M.K., C.G.-M.; funding acquisition, M.K., C.G.-M. All authors have read and agreed to the published version of the manuscript.

**Funding:** This research was funded by Research Fund for Coal and Steel, grant number RFCS-2016-754070.

**Conflicts of Interest:** The authors declare no conflict of interest. The funders had no role in the design of the study; in the collection, analyses, or interpretation of data; in the writing of the manuscript, or in the decision to publish the results.

#### References

1. Perez, M.; Sidoroff, C.; Vincent, A.; Esnouf, C. Microstructural evolution of martensitic 100Cr6 bearing steel during tempering: From thermoelectric power measurements to the prediction of dimensional changes. *Acta Mater.* **2009**, *57*, 3170–3181. [[CrossRef](#)]
2. Sourmail, T.; Caballero, F.G.; Moudian, F.; De Castro, D.; Benito, M. High hardness and retained austenite stability in Si-bearing hypereutectoid steel through new heat treatment design principles. *Mater. Des.* **2018**, *142*, 279–287. [[CrossRef](#)]
3. Hasan, H.S.; Peet, M.J.; Bhadeshia, H.K.D.H. Severe tempering of bainite generated at low transformation temperatures. *Int. J. Mater. Res.* **2012**, *103*, 1319–1324. [[CrossRef](#)]

4. Wang, D.; Chen, C.-W.; Dalton, J.C.; Yang, F.; Sharghi-Moshtaghin, R.; Kahn, H.; Ernst, F.; Williams, R.E.A.; McComb, D.W.; Heuer, A.H. "Colossal" interstitial supersaturation in delta ferrite in stainless steels—I. Low-temperature carburization. *Acta Mater.* **2015**, *86*, 193–207. [[CrossRef](#)]
5. Liu, D.; Bai, B.; Fang, H.; Zhang, W.; Gu, J.; Chang, K. Effect of tempering temperature and carbide free bainite on the mechanical characteristics of a high strength low alloy steel. *Mater. Sci. Eng. A* **2004**, *371*, 40–44. [[CrossRef](#)]
6. Bhadeshia, H.K.D.H. *Tempering of Bainite. Bainite in Steels*; IOM Communications: Geneva, Switzerland, 2001; pp. 91–116.
7. Peet, M.J.; Babu, S.S.; Miller, M.K.; Bhadeshia, H.K.D.H. Tempering of low-temperature bainite. *Metall. Mater. Trans. A* **2017**, *48*, 3410–3418. [[CrossRef](#)]
8. Garcia-Mateo, C.; Caballero, F.G. Bainitic steels: Tempering. In *Encyclopedia of Iron, Steel, and Their Alloys*; Taylor & Francis: Milton Park, Abingdon, UK, 2016; pp. 1–14. ISBN 1-4665-1104-4.
9. Caballero, F.G.; Miller, M.K.; Garcia-Mateo, C. The approach to equilibrium during tempering of a bulk nanocrystalline steel: An atom probe investigation. *J. Mater. Sci.* **2008**, *43*, 3769–3774. [[CrossRef](#)]
10. Garcia-Mateo, C.; Peet, M.; Caballero, F.G.; Bhadeshia, H.K.D.H. Tempering of hard mixture of bainitic ferrite and austenite. *Mater. Sci. Technol.* **2004**, *20*, 814–818. [[CrossRef](#)]
11. Hulme-Smith, C.N.; Lonardelli, I.; Peet, M.J.; Dippel, A.C.; Bhadeshia, H.K.D.H. Enhanced thermal stability in nanostructured bainitic steel. *Scr. Mater.* **2013**, *69*, 191–194. [[CrossRef](#)]
12. Santajuana, M.A.; Rementeria, R.; Kuntz, M.; Jimenez, J.A.; Caballero, F.G.; Garcia-Mateo, C. Low-Temperature bainite: A thermal stability study. *Metall. Mater. Trans. A Phys. Metall. Mater. Sci.* **2018**, *49*, 2026–2036. [[CrossRef](#)]
13. Saha Podder, A.; Bhadeshia, H.K.D.H. Thermal stability of austenite retained in bainitic steels. *Mater. Sci. Eng. A* **2010**, *527*, 2121–2128. [[CrossRef](#)]
14. Saha Podder, A. Tempering of a Mixture of Bainite and Retained Austenite. Ph.D. Thesis, University of Cambridge, Cambridge, UK, January 2011.
15. Kuntz, M.; Garcia-Mateo, C.; Garcia Caballero, F.; Ruiz-Jimenez, V.; Sourmail, T.; Lille, S.; Wicks, G.; Allain, S.; Denis, S.; Geandier, G.; et al. *Design of New Economic Secondary Precipitating Steels for Fatigue Resistance at Elevated Service Temperatures (STEELSECO-RFCS-754070)*; EUROPEAN COMMISSION Directorate G—Industrial Technologies, Unit, G.5—Research Fund for Coal and Steel, European Commission: Luxembourg, 2020.
16. Baker, R.G. The tempering of 2.25 Cr%-1% Mo steel after quenching and normalizing. *J. Iron Steel Inst.* **1959**, *192*, 257–268.
17. Irvine, K.J.; Pickering, F.B. Low-carbon bainitic steels. *J. Iron Steel Inst.* **1957**, *187*, 292–309.
18. Siwecki, T.; Eliasson, J.; Lagneborg, R.; Hutchinson, B. Vanadium Microalloyed Bainitic Hot Strip Steels. *ISIJ Int.* **2010**, *50*, 760–767. [[CrossRef](#)]
19. Garcia-Mateo, C.; Sourmail, T.; Caballero, F.G.; Smanio, V.; Kuntz, M.; Ziegler, C.; Leiro, A.; Vuorinen, E.; Elvira, R.; Teeri, T. Nanostructured steel industrialisation: Plausible reality. *Mater. Sci. Technol.* **2014**, *30*, 1071–1078. [[CrossRef](#)]
20. Sourmail, T.; Smanio, V.; Ziegler, C.; Heuer, V.; Kuntz, M.; Caballero, F.G.; Garcia-Mateo, C.; Cornide, J.; Elvira, R.; Leiro, A.; et al. *Novel Nanostructured Bainitic Steel Grades to Answer the Need for High-Performance Steel Components (Nanobain)*; RFSR-CT-2008-00022; EUROPEAN COMMISSION Directorate G—Industrial Technologies, Unit, G.5—Research Fund for Coal and Steel, European Commission: Luxembourg, 2013; ISBN 978-92-79-29234-7.
21. Garcia-Mateo, C.; Caballero, F.G.; Sourmail, T.; Smanio, V.; De Andres, C.G. Industrialised nanocrystalline bainitic steels. Design approach. *Int. J. Mater. Res.* **2014**, *105*, 725–734. [[CrossRef](#)]
22. Bhadeshia, H.K.D.H. *Bainite in Steels. Theory and Practice*; Maney Publishing: London, UK, 2015; ISBN 978-1-909662-74-2.
23. Balzar, D.; Audebrand, N.; Daymond, M.R.; Fitch, A.; Hewat, A.; Langford, J.I.; Le Bail, A.; Louër, D.; Masson, O.; McCowan, C.N.; et al. Size-strain line-broadening analysis of the ceria round-robin sample. *J. Appl. Crystallogr.* **2004**, *37*, 911–924. [[CrossRef](#)]
24. Cheng, L.; Brakman, C.M.; Korevaar, B.M.; Mittemeijer, E.J. The tempering of iron-carbon martensite: dilatometric and calorimetric analysis. *Metall. Trans. A* **1988**, *19*, 2415–2426. [[CrossRef](#)]

25. Lee, S.J.; Lusk, M.T.; Lee, Y.K. Conversional model of transformation strain to phase fraction in low alloy steels. *Acta Mater.* **2007**, *55*, 875–882. [[CrossRef](#)]
26. Stuart, H.; Rindley, N. Thermal expansion of cementite and other phases. *J. Iron Steel Inst.* **1966**, *204*, 711–717.
27. García De Andrés, C.; Caballero, F.G.; Capdevila, C.; Bhadeshia, H.K.D.H. Modelling of kinetics and dilatometric behavior of non-isothermal pearlite-to-austenite transformation in an eutectoid steel. *Scr. Mater.* **1998**, *39*, 791–796. [[CrossRef](#)]
28. Garcia-Mateo, C.; Caballero, F.G.; Capdevila, C.; de Andres, C.G. Estimation of dislocation density in bainitic microstructures using high-resolution dilatometry. *Scr. Mater.* **2009**, *61*, 855–858. [[CrossRef](#)]
29. Bhadeshia, H.K.D.H.; David, S.A.; Vitek, J.M.; Reed, R.W. Stress induced transformation to bainite in Fe–Cr–Mo–C pressure vessel steel. *Mater. Sci. Technol.* **1991**, *7*, 686–698. [[CrossRef](#)]
30. Dyson, D.J.; Holmes, B. Effect of alloying additions on the lattice parameter of austenite. *J. Iron Steel Inst.* **1970**, *208*, 469–474.
31. Moyer, J.M.; Ansell, G.S. The volume expansion accompanying the martensite transformation in iron-carbon alloys. *Metall. Trans. A* **1975**, *6*, 1785–1791. [[CrossRef](#)]
32. Materials, A.S. *Annual Book of ASTM Standards: Vol. 03.01, Metals-Mechanical Testing; Elevated and Low Temperature Tests, Metallography; Metals Test Methods and Analytical Procedures*; American Society for Testing and Materials: West Conshohocken, PA, USA, 1999.
33. Laboratory, N.P. *MTDATA*; National physical Laboratory: Teddington, Middlesex, UK, 2003.
34. Bhadeshia, H.K.D.H.; Edmonds, D.V. The mechanism of bainite formation in steels. *Acta Metall.* **1980**, *28*, 1265–1273. [[CrossRef](#)]
35. Guo, L.; Bhadeshia, H.K.D.H.; Roelofs, H.; Lembke, M.I. In situ synchrotron X-ray study of bainite transformation kinetics in a low-carbon Si-containing steel. *Mater. Sci. Technol. (U. K.)* **2017**, *33*, 2147–2156. [[CrossRef](#)]
36. Garcia-Mateo, C.; Caballero, F.G.; Miller, M.K.; Jimenez, J.A. On measurement of carbon content in retained austenite in a nanostructured bainitic steel. *J. Mater. Sci.* **2012**, *47*, 1004–1010. [[CrossRef](#)]
37. Garcia-Mateo, C.; Jimenez, J.A.; Yen, H.-W.; Miller, M.K.; Morales-Rivas, L.; Kuntz, M.; Ringer, S.P.; Yang, J.-R.; Caballero, F.G. Low temperature bainitic ferrite: Evidence of carbon super-saturation and tetragonality. *Acta Mater.* **2015**, *91*, 162–173. [[CrossRef](#)]
38. Hulme-Smith, C.N.; Peet, M.J.; Lonardelli, I.; Dippel, A.C.; Bhadeshia, H.K.D.H. Further evidence of tetragonality in bainitic ferrite. *Mater. Sci. Technol. (U. K.)* **2015**, *31*, 254–256. [[CrossRef](#)]
39. Bhadeshia, H.K.D.H. Carbon in cubic and tetragonal ferrite. *Philos. Mag.* **2013**, *93*, 3714–3725. [[CrossRef](#)]
40. Jang, J.H.; Bhadeshia, H.K.D.H.; Suh, D.W. Solubility of carbon in tetragonal ferrite in equilibrium with austenite. *Scr. Mater.* **2013**, *68*, 195–198. [[CrossRef](#)]
41. Bhadeshia, H.K.D.H.; Edmonds, D.V. Bainite in silicon steels: New composition–property approach Part 1. *Met. Sci.* **1983**, *17*, 411–419. [[CrossRef](#)]
42. Bhadeshia, H.K.D.H.; Edmonds, D.V. The bainite transformation in a silicon steel. *Metall. Trans. A* **1979**, *10*, 895–907. [[CrossRef](#)]
43. Sandvik, B.P.J. The Bainite reaction in Fe-Si-C Alloys: The primary stage. *Metall. Trans. A* **1982**, *13*, 777–787. [[CrossRef](#)]
44. Tanino, M.; Nishida, T. On the secondary hardening on tempering in vanadium steels. *Trans. Jpn. Inst. Met.* **1968**, *9*, 103–110. [[CrossRef](#)]
45. Lagneborg, R.; Siwecki, T.; Zajac, S.; Hutchinson, B. Role of vanadium in microalloyed steels. *Scand. J. Metall.* **2001**, *28*, 58–59.
46. Baker, T.N. Processes, microstructure and properties of vanadium microalloyed steels. *Mater. Sci. Technol.* **2009**, *25*, 1083–1107. [[CrossRef](#)]
47. Podder, A.S.; Lonardelli, I.; Molinari, A.; Bhadeshia, H.K.D.H. Thermal stability of retained austenite in bainitic steel: An in situ study. *Proc. R. Soc. A Math. Phys. Eng. Sci.* **2011**, *467*, 3141–3156. [[CrossRef](#)]
48. Hasan, H.S.; Peet, M.J.; Avettand-Fénoël, M.-N.; Bhadeshia, H.K.D.H. Effect of tempering upon the tensile properties of a nanostructured bainitic steel. *Mater. Sci. Eng. A* **2014**, *615*, 340–347. [[CrossRef](#)]
49. Stewart, J.W.; Thomson, R.C.; Bhadeshia, H.K.D.H. Cementite precipitation during tempering of martensite under the influence of an externally applied stress. *J. Mater. Sci.* **1994**, *29*, 6079–6084. [[CrossRef](#)]
50. Bhadeshia, H.K.D.H. Theoretical analysis of changes in cementite composition during tempering of bainite. *Mater. Sci. Technol.* **1989**, *5*, 131–137. [[CrossRef](#)]

51. Bhadeshia, H.; Honeycombe, R. Tempering of martensite. In *Steels: Microstructure and Properties*; Elsevier: Amsterdam, The Netherlands, 2017; pp. 237–270. ISBN 9780081002704.
52. Yamasaki, S.; Bhadeshia, H.K.D.H. Modelling and characterisation of V<sub>4</sub>C<sub>3</sub> precipitation and cementite dissolution during tempering of Fe—C—V martensitic steel. *Mater. Sci. Technol.* **2003**, *19*, 1335–1343. [[CrossRef](#)]
53. Sourmail, T.; Smanio, V.; Caballero, F.G.; Cornide, J.; Capdevilla, C.; Garcia-Mateo, C. Evolution of microstructure and mechanical properties during tempering of continuously cooled bainitic steels. In *Materials Science Forum—Thermec 2011*; Trans Tech Publications Ltd.: Kapellweg, Switzerland, 2012; pp. 706–709. ISBN 9783037853030.
54. Grajcar, A.; Morawiec, M.; Jimenez, J.A.; Garcia-Mateo, C. Dilatometric and microstructural study of martensite tempering in 4% mn steel. *Materials* **2020**, *13*, 4442. [[CrossRef](#)] [[PubMed](#)]
55. Caballero, F.G.; Miller, M.K.; Garcia-Mateo, C.; Capdevila, C.; Babu, S.S. Redistribution of alloying elements during tempering of a nanocrystalline steel. *Acta Mater.* **2008**, *56*, 188–199. [[CrossRef](#)]
56. Caballero, F.G.; Miller, M.K.; Garcia-Mateo, C. Atom Probe Tomography Analysis of Precipitation during Tempering of a Nanostructured Bainitic Steel. *Metall. Mater. Trans. A* **2011**, *42*, 3660–3668. [[CrossRef](#)]
57. Caballero, F.G.; Miller, M.K.; Clarke, A.J.; Garcia-Mateo, C. Examination of carbon partitioning into austenite during tempering of bainite. *Scr. Mater.* **2010**, *63*, 442–445. [[CrossRef](#)]
58. Caballero, F.G.; Garcia-Mateo, C.; García De Andrés, C. Dilatometric study of reaustenitisation of high silicon bainitic steels: Decomposition of retained austenite. *Mater. Trans.* **2005**, *46*, 581–586. [[CrossRef](#)]
59. Talebi, S.; Ghasemi-Nanasa, H.; Jahazi, M.; Melkonyan, H. In situ study of phase transformations during non-isothermal tempering of bainitic and martensitic microstructures. *Metals* **2017**, *7*, 346. [[CrossRef](#)]
60. Talebi, S.; Jahazi, M.; Melkonyan, H. Retained austenite decomposition and carbide precipitation during isothermal tempering of a medium-carbon low-alloy bainitic steel. *Materials* **2018**, *11*, 1441. [[CrossRef](#)]
61. Caballero, F.G.; Miller, M.K.; Babu, S.S.; Garcia-Mateo, C. Atomic scale observations of bainite transformation in a high carbon high silicon steel. *Acta Mater.* **2007**, *55*, 381–390. [[CrossRef](#)]
62. Kalish, D.; Cohen, M. Structural changes and strengthening in the strain tempering of martensite. *Mater. Sci. Eng. A* **1970**, *6*, 156–166. [[CrossRef](#)]
63. He, S.H.; He, B.B.; Zhu, K.Y.; Huang, M.X. Evolution of dislocation density in bainitic steel: Modeling and experiments. *Acta Mater.* **2018**, *149*, 46–56. [[CrossRef](#)]

**Publisher's Note:** MDPI stays neutral with regard to jurisdictional claims in published maps and institutional affiliations.



© 2020 by the authors. Licensee MDPI, Basel, Switzerland. This article is an open access article distributed under the terms and conditions of the Creative Commons Attribution (CC BY) license (<http://creativecommons.org/licenses/by/4.0/>).